NASA TECHNICAL MEMORANDUM

NASA TM X-2091

NASA TM X-2091

ESTIMATED AERODYNAMICS OF ALL-BODY HYPERSONIC AIRCRAFT CONFIGURATIONS

by Louis J. Williams

Office of Advanced Research and Technology
Mission Analysis Division
Moffett Field, Calif. 94035

NATIONAL AERONAUTICS AND SPACE ADMINISTRATION • WASHINGTON, D. C. • MARCH 1971

1. Report No. NASA TM X-2091	2. Government Accession No.	3. Recipient's Catalog No.
4. Title and Subtitle ESTIMATED AERODYNAMICS OF ALL–BODY HYPERSONIC AIRCRAFT CONFIGURATIONS		5. Report Date March 1971 6. Performing Organization Code
7. Author(s) Louis J. Williams		8. Performing Organization Report No. A–3637
9. Performing Organization Name and Address Office of Advanced Research and Technology Mission Analysis Division Moffett Field, Calif. 94035		10. Work Unit No. 789–50–01–01–15 11. Contract or Grant No.
12. Sponsoring Agency Name and Address National Aeronautics and Space Administration Washington, D. C. 20546		13. Type of Report and Period Covered Technical Memorandum 14. Sponsoring Agency Code

15. Supplementary Notes

16. Abstract

The results of analyses for estimating the aerodynamics of a representative family of all-body hypersonic aircraft configurations are presented. The configuration body shape is a delta planform with an elliptical cone forebody and an elliptical cross-section afterbody. Semiempirical and theoretical predictions of the aerodynamic characteristics of the forebody are compared with available experimental data to show the reliability of the basic methods.

Results are presented for aerodynamic performance, surface temperatures, and static longitudinal and directional stability. Aerodynamic performance of the all-body configurations is presented in the form of the effect on complete configuration maximum lift-to-drag ratio of Mach number, configuration geometry, and maximum allowable leading-edge temperature. Variations in the basic all-body shape were investigated using three independent shape parameters; body leading-edge sweep, position of breakpoint between forebody and afterbody, and ratio of maximum cross section to body planform area. The third shape parameter had the strongest influence on the aerodynamic performance.

Studies of the radiation equilibrium surface temperature show that the temperatures on the lower surface resulting from the inherent low lift loading of the all-body configuration are less than would be expected for higher lift-loading configurations. A brief analysis of vehicle stability and control showed that using a canard for trim instead of horizontal fins reduced trim drag penalties.

17. Key Words (Suggested by Author(s)) Aerodynamics All-Body Hypersonic Aircraft		18. Distribution Statement Unclassified–Unlimited	
19. Security Classif. (of this report) Unclassified	20. Security Classif. (of this page) Unclassified	21. No. of Pages 37	22. Price* $3.00

*For sale by the National Technical Information Service, Springfield, Virginia 22151

SYMBOLS

a	speed of sound, ft/sec
a_o	speed of sound at sea level, ft/sec
$\frac{a}{b}$	major/minor axis ratio of forebody elliptical cross sections
AR	aspect ratio, $\frac{\text{span}^2}{\text{plan area}}$
b_{FIN}	fin span, ft
C_1	coefficient multiplying $\sin \alpha$ in C_L expression
C_2	coefficient multiplying $\sin^2 \alpha$ in C_L expression
$C_{D_{BB}}$	bluntness drag coefficient for body (nose)
$C_{D_{BF}}$	bluntness drag coefficient for fins (leading edges)
$C_{D_{FB}}$	friction drag coefficient for body
$C_{D_{FF}}$	friction drag coefficient for fins
C_{D_i}	induced drag coefficient
C_{D_o}	zero-lift drag coefficient
$C_{D_{OB}}$	zero-lift drag coefficient for body
$C_{D_{OF}}$	zero-lift drag coefficient for fins
$C_{D_{pB}}$	pressure drag coefficient for body
$C_{D_{pF}}$	pressure drag coefficient for fins
C_{D_X}	drag coefficient of type X
$C_{D_{X_F}}$	drag coefficient of type X for fins

C_L	lift coefficient
$C_{m_{CG}}$	moment coefficient about body center of gravity
C_p	pressure coefficient
$C_{p_{2\text{-}D}}$	two-dimensional truncated base pressure coefficient
$C_{p_{BASE}}$	pressure coefficient on configuration afterbody
e	base of natural logarithms
h	altitude, ft
K_M	Mach number coefficient for C_{D_i} equation
l	body length, ft
l_π	forebody length, ft
$\left(\frac{L}{D}\right)_{MAX}$	maximum $\frac{\text{lift}}{\text{drag}}$ ratio
$\frac{L}{S}$	planform lift loading, lb/ft^2
M	Mach number
$(MAC)_{BODY}$	mean aerodynamic chord of body, ft
$(MAC)_{FIN}$	mean aerodynamic chord of fin, ft
M_{CRIT}	critical Mach number for Mach cone intersection with forebody surface $\left(\sqrt{1+\left(\frac{4}{AR}\right)^2} \quad \text{for } \frac{a}{b} \geqslant 1.0\right)$
M_{MAX}	Mach number for maximum nose and fin leading-edge radiation equilibrium temperature
M_o	free-stream Mach number
M_{SA}	Mach number for shock attachment to leading edge

q	dynamic pressure, lb/ft^2
Re	Reynolds number
$r_{LE_{FIN}}$	fin leading-edge radius, ft
r_{NOSE}	nose radius, ft
S	planform area, ft^2
S_π	maximum cross-sectional area, ft^2
S_{CA}	canard planform area, ft^2
S_{FIN}	fin planform area, ft^2
S_{HT}	total horizontal fin planform area, ft^2
S_{REF}	reference area used in aerodynamic coefficients (body planform area), ft^2
S_{VT}	total vertical fin profile area, ft^2
S_{WET}	wetted surface area, ft^2
$\left(S_{WET}\right)_{FIN}$	wetted surface area of fin, ft^2
$\left(\frac{t}{c}\right)_{BODY}$	thickness ratio of body
$\left(\frac{t}{c}\right)_{FIN}$	thickness ratio of fin
T_{LE}	leading-edge radiation equilibrium temperature, °R
W_{GTO}	gross takeoff weight, lb
x	length of boundary-layer run used in Re, ft
$\frac{y}{a}$	semispan station (length from centerline/semispan)
α	angle of attack, deg

β	compressibility factor $(\lvert M^2 - 1\rvert)^{1/2}$
γ	ratio of specific heats
δ	deflection angle, deg
δ_{CA}	canard deflection angle with respect to body (positive = leading edge up), deg
δ_{HT}	horizontal fin deflection angle with respect to body (positive = leading edge up), deg
ϵ	emissivity
ϵ_{SKIN}	surface emissivity
θ_B	included angle of body, deg
λ	fin taper ratio
Λ	leading-edge sweep angle, measured from axis perpendicular to body centerline, deg
Λ_{FIN}	fin leading-edge sweep angle, deg
μ_o	free-stream coefficient of viscosity, lb sec/ft^2
ρ	density, slugs/ft^3
ρ_G	gross body density (gross takeoff weight/theoretical body volume), lb/ft^3
ρ_o	free-stream air density, slugs/ft^3
ρ_{SL}	sea-level air density, slugs/ft^3
$\dfrac{\partial C_{m_{CG}}}{\partial \alpha}$	partial derivative of $C_{m_{CG}}$ with respect to α, 1/deg

ESTIMATED AERODYNAMICS OF ALL–BODY HYPERSONIC AIRCRAFT CONFIGURATIONS

Louis J. Williams

Office of Advanced Research and Technology
Mission Analysis Division
Moffett Field, California 94035

SUMMARY

The results of analyses for estimating the aerodynamics of a representative family of all-body hypersonic aircraft configurations are presented. The configuration body shape is a delta planform with an elliptical cone forebody and an elliptical cross-section afterbody. Semiempirical and theoretical predictions of the aerodynamic chracteristics of the forebody are compared with available experimental data to show the reliability of the basic methods. Areas in the aerodynamic analysis lacking in proven analytical prediction methods or experimental data are noted.

Results are presented for aerodynamic performance, surface temperatures, and static longitudinal and directional stability. Aerodynamic performance of the all-body configurations is presented in the form of the effect on complete configuration maximum lift-to-drag ratio of Mach number, configuration geometry, and maximum allowable leading-edge temperature. The effect due to configuration geometry, particularly the body shape, was most pronounced. Variations in the basic all-body shape were investigated using three independent shape parameters; body leading-edge sweep, position of breakpoint between forebody and afterbody, and ratio of maximum cross section to body planform area. The third shape parameter had the strongest influence on the aerodynamic performance.

Studies of the radiation equilibrium surface temperature show that the temperatures on the lower surface resulting from the inherent low lift loading of the all-body configuration are less than would be expected for higher lift-loading configurations. Vehicle stability was analyzed briefly to obtain nominal required horizontal and vertical fin sizes for the aerodynamic performance calculations. This analysis also showed that using a canard for trim instead of horizontal fins reduced trim drag penalties.

INTRODUCTION

Hypersonic aircraft powered by hydrogen-fueled scramjet propulsion systems have shown potentially high performance for both cruise and boost missions. A characteristic of these aircraft is a large-volume fuselage required for the low-density hydrogen fuel. Attempts to optimize these configurations have resulted in various degrees of wing and fuselage blending. The limit of this blending is a wingless configuration in which the fuselage provides all the lift.

As part of a mission analysis of such all-body configurations, the estimation of their aerodynamics was investigated. For the purposes of a parametric study, simplified aerodynamic calculation methods and a simply defined configuration shape were used. The configurations are of delta planform with an elliptical cone forebody and an elliptical cross-section afterbody. A given configuration was specified by the values of three independent body shape parameters: the sweepback of the body leading edge; the position of the breakpoint between the forebody and afterbody; and the ratio of the maximum cross section to body planform area. Results are presented in terms of the maximum lift-to-drag ratio for complete configurations including fins.

In conjunction with the aerodynamic analyses, the vehicle stability and surface temperatures at hypersonic speed were studied. The important equations used in the aerodynamic calculations are given in an appendix.

CONFIGURATION

Figure 1 compares an all-body configuration and a typical wing-body configuration. With the simply defined, all-body configuration shown on the right in figure 1, shape changes are specified by varying major shape parameters, thus facilitating the aerodynamic calculations.

The nominal configuration studied is shown in figure 2. The body has a delta planform, with an elliptical cone forebody and an elliptical cross-section afterbody that forms a smooth transition surface from the end of the forebody to a straight-line trailing edge. The shape is specified by three independent parameters: (1) The sweepback of the body leading edge, Λ; (2) the position of the breakpoint between the forebody and afterbody, specified as the breakpoint length ratio, l_π/l; and (3) the fatness ratio specified as the ratio of the maximum cross-section area to the total planform area S_π/S. For l_π/l values greater than 0.5 the longitudinal location of maximum cross-section area and breakpoint coincide. The nominal vehicle shape shown in figure 2 ($\Lambda = 75°$, $l_\pi/l = 0.667$, $S_\pi/S = 0.0935$) does not represent an optimum or preferred configuration, but was selected as a base point for the parametric studies.

The fatness ratio parameter was chosen so that the effect of changes in sweep angle and breakpoint length ratio would not be dominated by a change in the frontal area. The algebraic relationship between the shape parameters chosen and the forebody cross-section ellipse ratio a/b is shown in figure 3. For constant fatness ratio, the forebody ellipse ratio varies with the square of the breakpoint length ratio and the cotangent of the sweep.

In addition to variations of the shape parameters, parametric variations of the gross takeoff weight, gross body density (defined as gross weight divided by theoretical body volume), maximum allowable leading-edge radiation equilibrium temperature, and control surface size were performed. The nominal gross weight was 500,000 pounds and the gross body density was 7.0 pounds per cubic foot. This corresponds to a theoretical body volume of 71,400 cubic feet.

METHODS OF ESTIMATING AERODYNAMICS

Lift

The basic configuration aerodynamics were calculated using a computer program which incorporated the equations outlined in the appendix. The lift (and induced drag) equations for the basic body were estimated by means of nonlinear relations similar to those used in reference 1 for a delta wing. These equations were developed by curve fitting data for low aspect ratio wings from references 2, 3, and 4 and applying Gothert's rule or shock-expansion theory, where applicable. The coefficients used in these equations were modified to account for the rounded leading edge of the all-body configuration, which causes linear subsonic variation of the elliptic-cone lift coefficient as opposed to the significant nonlinear variation present for the sharp leading edge of a delta wing. This comparison is shown in figure 4 for a Mach number of 0.6; the effect of Mach number on the estimated elliptic cone lift coefficient is also shown. These curves agreed well with experimental data from reference 5. Figure 5 shows the effect of shape on the estimated lift coefficient; also shown are experimental data from reference 6 which show agreement. At present, experimental data are available only for the elliptical cone forebody. The estimation equations used depend only on planform shape, but agree well with thick or thin elliptical cone shapes. Therefore, the effect of the body thickness distribution of the all-body configuration on the lift curve is neglected.

Induced Drag

The induced drag relation used the equation for the sharp leading-edge delta wing modified by a coefficient to account for the rounded leading edge of the elliptic cone, which resulted in leading-edge suction subsonically. The effect of shape on the induced drag and a comparison with experimental data are given in figure 6. The effect of Mach number on the induced drag is shown in figure 7. These curves correlated well with experimental data.

Zero-Lift Body Drag

The zero-lift drag coefficient C_{D_0} of the basic body was obtained by adding the pressure (or wave), skin friction, and nose bluntness drag components. The Mach number range determined the method used to calculate each of these components.

Body pressure drag– Subsonically ($M \leqslant 0.8$), the pressure drag was assumed zero; normally this term would be small and the hypersonic vehicle mission performance is relatively insensitive to subsonic drag because of small loiter time subsonically. Transonically ($0.8 < M < 1.2$), the pressure drag was assumed to vary linearly with Mach number.

Supersonically ($1.2 \leqslant M \leqslant M_{CRIT}$), the wave drag was obtained by numerical integration of the body pressure distribution. For $M \leqslant M_{CRIT}$ (the critical Mach number for the intersection of the Mach cone with the forebody surface), the forebody pressure distribution was calculated by the second-order elliptic cone equations developed by Van Dyke (ref. 7). The resulting forebody pressure distributions for elliptic cones with two values of a/b are compared in figure 8 with experimental data from reference 6. The cross section of each elliptic cone is shown above the corresponding data. The agreement with experimental data is excellent. The afterbody pressure distribution was estimated by assuming a Prandtl-Meyer expansion from the forebody pressures at the breakpoint. As indicated in figure 9, the expansion angle was determined from cross sections taken along rays emanating from the body nose. Note that xy is a straight line along the afterbody; this follows because the afterbody is composed of elliptic cross sections whose major and minor axes vary linearly with body length. The pressure distribution on the afterbody was obtained by calculating the Prandtl-Meyer expansion of the forebody pressure through the appropriate expansion angle δ at the breakpoint of each ray.

Hypersonically ($M \geqslant 12$), the forebody pressure distribution was obtained using pure Newtonian theory. The afterbody pressure distribution was obtained in the same manner as in the supersonic calculations. The Mach numbers of the forebody flow were estimated from the free-stream conditions and forebody Newtonian pressures using the oblique shock relations. Between the regions of applicability of the previously described supersonic and hypersonic methods ($M_{CRIT} < M < 12$), the forebody pressure coefficient was assumed to vary as the square of the Mach number from the Van Dyke ($M = M_{CRIT}$) value to the Newtonian ($M = 12$) value.

Body base drag– Normally, the afterbody pressure drag was computed using the pressure distribution obtained by the Prandtl-Meyer expansion technique previously described. However, each pressure coefficient on the afterbody was checked with the separated flow, turbulent boundary layer, two-dimensional base pressure coefficient obtained from reference 8. If the Prandtl-Meyer pressure coefficient was lower, the flow was assumed to separate over that portion of the afterbody and the two-dimensional pressure coefficient was used. To facilitate programming, an equation was obtained by curve fitting the data for two-dimensional base pressures. This equation is given in the appendix.

Body friction drag– Subsonically ($M \leqslant 0.8$), the friction drag of the body was calculated using a relation previously developed for the delta wing (ref. 9), which is based on turbulent boundary layer, flat-plate skin friction and contains an empirical correction for thickness induced pressure fields. The basic equation is Frankl and Voishel's extension of Von Kármán's mixing-length hypothesis to compressible flow, and the empirical correction for thickness-induced pressure fields is the result of a correlation in reference 10 of a large amount of data.

Transonically ($0.8 < M < 1.2$), the skin friction was assumed to vary linearly with Mach number from the subsonic value at $M = 0.8$ to the $M = 1.2$ value. Supersonically and hypersonically ($M \geqslant 1.2$), the skin friction was obtained by numerical integration of the local skin-friction coefficient distribution. The local skin-friction coefficients were obtained using Eckert's reference enthalpy technique (ref. 11) for turbulent flow.

Figure 10 compares experimental data from reference 6 with the above methods for pressure and friction drag. Experimental data were available only for the elliptic cone forebody. There are no experimental data with which to verify the afterbody aerodynamic estimates. Because of the large transonic drag of the all-body configurations the acquisition of this type of experimental data is highly desirable. For purposes of comparison theoretical estimates were calculated for the forebody alone based on the flow parameters of the experiment. The experimental pressure drag was determined from surface pressure measurements. The total forebody drag was obtained experimentally from axial-force balance measurements with the base drag (computed from base pressure measurements) subtracted.

Body bluntness drag– The body nose was hemispherical with the radius calculated for a specified maximum radiation equilibrium temperature. An emissivity of 0.8 was assumed for all surface temperature calculations. The nominal nose maximum temperature was 4350° F. Subsonically ($0 \leqslant M \leqslant 0.8$) the bluntness drag was assumed to be zero. Transonically ($0.8 < M < 1.0$) it was assumed to increase linearly, with respect to Mach number, from zero to its supersonic value. At all supersonic Mach numbers ($M \geqslant 1.0$) the bluntness drag was estimated using the Newtonian flow approximation given in reference 12.

Zero-Lift Fin Drag

The zero-lift fin drag was added to the zero-lift drag of the body to obtain the total vehicle zero-lift drag coefficient. The fin drag was estimated by adding the pressure (or wave), friction, and leading-edge bluntness drag components. No trim drag penalties, vertical fin toe-in, or body-fin flow field interactions were included in the vehicle aerodynamics. All fin airfoils were hexagonal with the maximum thickness extending from the 30-percent chord location to the 70-percent chord location. The horizontal fin and canard dimensions were fixed by specifying the ratio of total fin area to body planform area. The vertical fin dimensions were fixed by specifying the ratio of total fin area to body profile area. The effect of changes in fin size was investigated in the parametric study. The nominal fin leading-edge sweeps, aspect ratios, taper ratios, and thickness ratios used correspond to the fin shapes shown in figure 2 for the nominal configuration. The values used are listed in table 1.

TABLE 1.– GEOMETRY OF FINS

Fin shape parameter	Horizontal fins	Vertical fins	Canard
Leading-edge sweep	55°	60°	50°
Aspect ratio	0.933	1.200	1.675
Taper ratio	.200	.400	.200
Thickness ratio	.040	.040	.040

Fin wave drag– The wave drag of each fin (horizontals, verticals, and canard) was calculated using the same set of equations. Subsonically ($M \leqslant 0.8$) the fin wave drag was assumed zero. Transonically ($0.8 < M < 1.0$), it was assumed to increase linearly, with respect to Mach number, from zero to its computed value at Mach number 1. The wave drag of the fin at Mach number 1 was estimated by means of an empirical equation from reference 10 obtained by correlation of a wide variety of wing data. At Mach numbers between 1 and that for shock attachment to the fin leading edge, the wave drag was found by linear interpolation, with respect to Mach number. At Mach numbers equal to or greater than the shock attachment Mach number, the wave drag was estimated by linear supersonic theory.

Fin friction drag– The fin skin-friction drag was obtained from a relationship for turbulent boundary layer, flat-plate skin friction corrected for the effects of pressure gradients. This equation, used for the fin friction drag over the entire Mach number range, is of the same form as that used to estimate the subsonic body friction drag. (The derivation of this equation was discussed previously in the section on body friction drag.)

Fin bluntness drag– The fin leading edges were cylindrical with the radius calculated for a nominal radiation equilibrium temperature of 4350° R at the specified leading-edge sweep. Subsonically ($0 \leqslant M \leqslant 0.8$), the bluntness drag was assumed to be zero. Transonically ($0.8 < M < 1.0$), it was assumed to increase linearly, with respect to Mach number, from zero to its supersonic value. At all Mach numbers greater than or equal to 1, the bluntness drag was estimated from the Newtonian flow approximation (ref. 12).

Zero-Lift Drag Breakdown

Figure 11 shows the breakdown of zero-lift drag versus Mach number for a typical body shape. At transonic and low supersonic Mach numbers the pressure drag of the body, particularly the afterbody component, is the dominant drag contributor. At higher Mach numbers, this contribution diminishes until, at hypersonic speeds, the body drag due to pressure and skin friction essentially equals that from fin and bluntness drag.

The drag in the transonic region estimated by fairing from Mach 0.8 to 1.2 was compared with data calculated by the supersonic area rule program, which computes the wave drag of an equivalent body using the method of Eminton and Lord (ref. 13). Within the constraints of the specified body shape coordinates, the program determines the optimum area distribution for which the wave drag is a minimum. The wave drag calculations from this program were added to the friction drag calculated by the present method. The all-body shape was input to this program as a wing by specifying airfoil coordinates at chord locations along the span. In figure 11, the circles shown are for a more precisely specified wing shape than the squares. Assuming some optimization of the body shape for transonic drag, the squares show good agreement with the theoretical estimation based on the present methods. In particular, the maximum level of transonic drag estimated by fairing to Mach 1.2 appears reasonable.

AERODYNAMIC RESULTS

The all-body aerodynamic estimates are presented in terms of the maximum lift-to-drag ratio $(L/D)_{MAX}$. This $(L/D)_{MAX}$ was computed for each Mach number at the altitude where lift was equal to gross takeoff weight minus the centrifugal force. The variation of $(L/D)_{MAX}$ with Mach number for the nominal configuration is shown in figure 12. The shape of this curve is typical for all the all-body configurations. The following parametric studies consider the change in $(L/D)_{MAX}$ at Mach numbers of 1.2, 6.0, and 12.0. The corresponding values of $(L/D)_{MAX}$ for the nominal configuration are shown by tick marks, which are also used to show the nominal values in subsequent figures.

Effect of Body Shape

The effects of the body shape parameters – sweep, fatness ratio, and breakpoint length ratio – were investigated parametrically. The change in $(L/D)_{MAX}$ with body shape is the result of a tradeoff between lift-curve slope, zero-lift drag, and induced drag. In each figure the primary factor causing the change in $(L/D)_{MAX}$ will be explained. As an aid to visualizing the changes in body shape that result from changes in each parameter, the corresponding forebody ellipse ratio will also be noted.

The effect of body leading-edge sweep is shown in figure 13. In the transonic region at a Mach number of 1.2 the $(L/D)_{MAX}$ decreases with increasing sweep primarily because of the decreasing lift-curve slope. At a Mach number of 6.0 the $(L/D)_{MAX}$ increases with increasing sweep because of the decreasing forebody wave drag. However, at the higher sweeps ($\Lambda > 83°$) the decrease in wave drag is less significant, and the $(L/D)_{MAX}$ falls off because of the more dominant decrease in lift-curve slope. At a Mach number of 12.0 the $(L/D)_{MAX}$ increases with increasing sweep due to the decreasing forebody wave drag.

Figure 14 shows the effect of fatness ratio. The fatness ratio, ratio of the maximum body cross-section area to planform area, translates directly into the ratio of drag-producing frontal area to lift-producing planform area. Hence, for all Mach numbers, increasing fatness ratio results in increasing zero-lift drag and drastically decreasing $(L/D)_{MAX}$.

The effect of breakpoint length ratio is shown in figure 15. For all Mach numbers, increasing the breakpoint length ratio results in decreasing forebody wave drag and increasing afterbody pressure drag. Because the afterbody pressure drag is a larger percentage of the overall drag at the lower Mach numbers, the increase in $(L/D)_{MAX}$ with increasing breakpoint length ratio is not as rapid as for the higher Mach numbers.

Effect of Vehicle Size

The effect of vehicle takeoff weight is shown in figure 16 for the nominal configuration geometry with a fixed gross body density of 7 pounds per cubic foot. For reference, the corresponding vehicle length is also shown. The $(L/D)_{MAX}$ increases with increasing gross takeoff weight because the skin-friction drag coefficient decreases with increasing Reynolds number. The change is less significant at the lower Mach numbers where the skin friction is a smaller percentage of the overall drag. The effect of size is also strongest for small vehicles (less than 500,000 pounds gross takeoff weight) where the assumption of completely turbulent skin friction (which penalizes the smaller vehicle) is less reasonable. This consideration would be of importance only for research vehicles.

The effect of gross body density for the nominal vehicle at the fixed nominal gross takeoff weight of 500,000 pounds is shown in figure 17. Again, the corresponding vehicle length is shown for reference. The $(L/D)_{MAX}$ decreases slightly with increasing body density because the skin-friction drag coefficient increases with decreasing Reynolds number. Unique to the all-body configuration is the interdependence of gross takeoff weight, gross body density, and planform lift loading (or wing loading). Hence, for a given gross body density and body shape, the wing loading will change with changes in gross takeoff weight.

Effect of Maximum Allowable Temperature

The effect of maximum allowable leading edge and nose radiation equilibrium temperature is shown in figure 18. The temperature shown is the specified maximum temperature for sizing the body nose, horizontal fin leading edge, vertical fin leading edge, and canard leading-edge radii. For reference, the corresponding nose radius is also shown. The increase in $(L/D)_{MAX}$ with increasing allowable temperature is the result of decreasing bluntness drag (radius). The bluntness drag is a more significant proportion of the overall drag at the higher Mach numbers.

Effect of Fin Sizes

The nominal sizes for the horizontal fins, vertical fins, and canard were estimated to provide adequate stability and control as discussed in a later section. As mentioned previously, only the zero-lift drag (wave, friction, and bluntness) of the fins was included in the $(L/D)_{MAX}$ calculations. No trim drag or vertical fin toe-in penalties were included. The effect of horizontal fin, vertical fin, and canard size on configuration $(L/D)_{MAX}$ is shown in figures 19 to 21, respectively. The fin planform and shape parameters are included on each figure for reference. Each figure shows the loss in $(L/D)_{MAX}$ incurred for larger fin sizes.

SURFACE TEMPERATURES

A brief analysis of the vehicle surface radiation equilibrium temperatures was performed in conjunction with the study of configuration aerodynamics. The surface temperature distribution, at zero angle of attack, and the effects of Mach number, lift loading, and altitude on the surface temperature were investigated.

Surface Temperature Distribution

The surface radiation equilibrium temperature distribution was calculated at zero angle of attack only using the pressure distribution obtained for the zero-lift drag computation. The temperatures were estimated using Eckert's reference enthalpy technique for a turbulent boundary layer. The planform temperature contours for a typical configuration are shown in figure 22. The case shown is for a Mach number of 12 and an altitude of 115,000 feet. The configuration shape parameters and length are shown for reference.

Surface Temperature Variations

The effect of planform lift loading on surface radiation equilibrium temperature was estimated from calculations for a wedge with the same included angle as the forebody at the centerline of the all-body configuration. The upper and lower surface temperatures were calculated for the wedge angle of attack that resulted in the same planform lift loading as the all-body configuration. These temperatures were estimated using the reference enthalpy method and are assumed to represent the average spanwise temperature of the configuration. The planform lift loading of the configuration and the wedge were matched using computed values of surface pressures. The pressure on the wedge lower surface was computed by Newtonian theory and the corresponding Mach number was obtained by the oblique shock relations. The pressure on the wedge upper surface was computed using Newtonian theory when inclined toward the flow or a Prandtl-Meyer expansion when inclined away from the flow.

The upper and lower surface radiation equilibrium temperatures 25 feet aft of the wedge leading edge are shown versus Mach number in figure 23. The curves represent conditions for the nominal vehicle, which has a forebody wedge included angle of 7.65°. Curves are shown for several values of lift loading computed at a constant dynamic pressure of 1000 lb/ft^2. A typical value of lift loading is 30 lb/ft^2, corresponding to the nominal configuration in cruise. The reduction in lower surface temperature achieved by lower lift loadings is accompanied by a corresponding increase in upper surface temperature. Figure 24 shows the effects of cruise altitude and lift loading for a constant Mach number. Lift loading, rather than angle of attack, is used as a parameter because equilibrium cruise flight requires a given value of lift loading, which, to a first order, is independent of cruise altitude; whereas the angle of attack for equilibrium cruise flight varies widely with cruise altitude. The trends in the figure, however, can best be understood as the result of a tradeoff between altitude and angle of attack. For a fixed angle of attack increasing altitude causes decreasing surface temperature. This effect is most apparent for a lift loading of zero, where the lower surface angle to the free stream remains at 3.83°. For a fixed altitude, increasing angle of attack (or, equivalently, increasing the lift loading) causes increasing surface temperature. This effect is also shown in the figure for any of the constant altitude lines. At the lower altitudes, the angle of attack required to produce a lift loading of 40 lb/ft^2 is smaller (less than 1° at 80,000 ft) than at the higher altitudes (almost 15° at 160,000 ft). Hence, the effect of changes in the lift loading on surface temperature is greater at the higher altitudes. It is also significant that at the higher values of lift loading and altitude the lower surface temperature is virtually insensitive to altitude changes. At these conditions the upper surface pressure is essentially a vacuum and the lower surface pressure is approximately equal to the lift loading regardless of altitude. Since, at a constant flight Mach number, the heat-transfer rate to the lower surface is primarily a function of the lower surface pressure, the result is a nearly constant lower surface temperature independent of cruise altitude.

The foregoing discussion is based on the assumption that the wedge temperatures computed by the lift-loading analogy are representative of the average spanwise distribution of the all-body surface temperatures.

STABILITY

A preliminary stability analysis was performed to estimate the static longitudinal and directional stability at hypersonic speed. The moment coefficients were referenced about the body center of gravity with the body mean aerodynamic chord as the reference length. The body center-of-gravity location was determined by assuming constant body density. This appears to be a good assumption for a hydrogen-fueled vehicle since the gross density of the hydrogen tankage and the passenger compartment are both about 5 lb/ft^3. During a mission it may be advantageous to sequence the fuel tank usage to obtain the best center-of-gravity location corresponding to flight conditions. The body lift and drag were calculated using the methods previously described and were assumed to act through the planform center of area. The accuracy of this assumption depends on the configuration and flight conditions. For a thick (low a/b ratio) configuration at low angles of attack, the forebody may provide most of the aerodynamic forces, and hence, the center of pressure may act closer to the forebody planform center of area. Because of the lack of experimental or analytical data this effect was neglected for the present study. The lift and drag of the fins were estimated by Newtonian theory neglecting any effects of the body flow field (i.e., no interference forces were considered).

Longitudinal Stability

The longitudinal stability for the nominal configuration at a Mach number of 12 is shown in figure 25. The increase in stability due to the horizontal fins and canard is shown. Nominally, the canard was designed as a floating canard (the angle of attack of the canard remained fixed with respect to the free stream for all configuration angles of attack). The decrease in stability that results from a fixed canard is also shown. These data show that the configuration would maintain positive stability if the canard were to become locked.

Control Effectiveness

The control power of the horizontal fins is shown in figure 26 for the nominal horizontal fin size, which is 12.5 percent of the body plan area. Because of the relatively short moment arm between the horizontal fin location and the configuration center of gravity, the horizontal fin effectiveness for trim is impaired. The canard location is slightly more advantageous. Figure 27 shows the control power of the floating canard for the nominal canard size, corresponding to 4 percent of the body plan area. The floating canard possesses the ability to trim the configuration at the desired angle of attack while adding a positive lift increment to the configuration aerodynamics. The nominal configuration can be trimmed at $(L/D)_{MAX}$ with the floating canard at 15.6° angle of attack with respect to the free stream. To trim with the horizontal fins requires −9.5° fin angle of attack with respect to the free stream ($\delta_{HT} = -18.5°$). The use of the canard for trim results in a 0.37 percent decrease in untrimmed $(L/D)_{MAX}$ at cruise as compared to a 13.25 percent decrease when the horizontal fins are used.

Effect of Body Shape

Under the assumption of constant body density the body center-of-gravity location depends on the configuration breakpoint-length ratio and is independent on the sweep and fatness ratios. The center of gravity moves rearward with increasing breakpoint-length ratio. The effect of this shift in center-of-gravity location on the basic body longitudinal stability at hypersonic speeds is shown in figure 28. At the higher values of breakpoint-length ratio the center of gravity is behind the aerodynamic center (assumed at the planform center of area) and the basic body is unstable. The rearward center-of-gravity shift also results in a shorter moment arm for control with the horizontal fins. Therefore, configurations with higher values of breakpoint-length ratio may require larger horizontal fins to provide adequate longitudinal stability and control. However, engine forces, flow-field effects, and the actual location of the body center of pressure must be considered in a complete stability analysis.

Directional Stability

A preliminary directional stability analysis was performed for hypersonic speeds to estimate the required vertical fin size. To approximate the body contribution a representative analytical model, as shown in figure 29, was used. This model has a flat-sided body with one-half the included planform angle of the original configuration as shown by the dashed lines in the figure. (Note that this corresponds to a new body sweep angle equal to 45° plus one-half the original sweep.) The flat sided area of the model is equal to the cross-section area obtained by cutting the original body in the vertical plane at the new body sweep angle. Body side forces and vertical fin forces on the model were estimated by simple Newtonian theory. The computations indicated that the nominal configuration (with the nominal vertical fin size) was directionally stable hypersonically for a vertical fin flare of 5° included angle. This vertical fin flare results in a negligible (less than 0.5 percent) decrease in the configuration $(L/D)_{MAX}$ at Mach 12. Directional stability, for the nominal configuration, can also be obtained by a vertical fin toe-in of 5°; however, this results in a larger (approximately 1 percent) decrease in configuration $(L/D)_{MAX}$ at a Mach number of 12.

CONCLUDING REMARKS

The results of semiempirical and theoretical predictions of the aerodynamic characteristics of the forebody of all-body configurations have been compared with available experimental data. The good agreement obtained lends credence to the application of the basic analysis techniques to the entire all-body configuration. The degree to which these estimates represent the physical facts must await experimental data on the configurations studied. Such data will also be helpful in providing improvements in semiempirical and, perhaps, analytical prediction methods. Additional configuration studies are required with different geometric shapes to analyze the effect of the rounded leading edge and the forebody-afterbody ridge line of the present configuration family. Several critical problem areas requiring improved analytical techniques or experimental data include the pressure distribution at angle of attack, the high transonic drag, and the flow interaction effects on stability.

National Aeronautics and Space Administration
Moffett Field, California, 94035, April 23, 1970

APPENDIX

AERODYNAMICS EQUATIONS

LIFT

$$C_L = C_l \sin \alpha + C_2 \sin^2 \alpha$$

where

$$M \leq 1.0 \quad \left\{ \begin{array}{l} C_l = \dfrac{\pi AR}{2} - 0.355\ \beta^{0.45} AR^{1.45} \\ C_2 = 0 \end{array} \right.$$

$$\begin{array}{l} M > 1.0 \\ \beta < \dfrac{4}{AR} \end{array} \quad \left\{ \begin{array}{l} C_l = \dfrac{\pi AR}{2} - 0.153\ \beta AR^2 \\ C_2 = \text{linear interpolation with respect to } \beta \text{ from} \\ \qquad C_2 = 0 \text{ at } \beta = 0 \text{ to} \\ \qquad C_2 = e^{[0.955-(4.35/M)]} \text{ at } \beta = \dfrac{4}{AR} \end{array} \right.$$

$$\begin{array}{l} M > 1.0 \\ \beta \geq \dfrac{4}{AR} \end{array} \quad \left\{ \begin{array}{l} C_l = \dfrac{4.17}{\beta} - 0.13 \\ C_2 = e^{[0.955-(4.35/M)]} \end{array} \right.$$

INDUCED DRAG

$$C_{D_i} = K_M C_L \tan \alpha$$

where

$$M < 3.0 \quad \left\{ \ K_M = 0.25\ (1 + M) \right.$$

$$M \geq 3.0 \quad \left\{ \ K_M = 1.0 \right.$$

ZERO-LIFT BODY DRAG

$$C_{D_{OB}} = C_{D_{pB}} + C_{D_{FB}} + C_{D_{BB}}$$

Body Pressure Drag

$$M \le 0.8 \quad \left\{ C_{D_{pB}} = 0 \right.$$

$$0.8 < M < 1.2 \quad \left\{ \begin{array}{l} C_{D_{pB}} = \text{linear interpolation with respect to } M \text{ from} \\ \qquad C_{D_{pB}} = 0 \quad \text{at} \quad M = 0.8 \quad \text{to} \\ \qquad C_{D_{pB}} = C_{D_{pB}} \quad \text{at} \quad M = 1.2 \end{array} \right.$$

$$M \ge 1.2 \quad \left\{ \begin{array}{l} C_{D_{pB}} = C_{D_{pB}} \text{ from numerical integration of pressure} \\ \qquad \text{distribution on body} \end{array} \right.$$

Body Base Drag

$C_{p_{BASE}} = C_p$ from Prandtl-Meyer expansion of forebody pressure distribution

Unless $C_p < C_{p_{2-D}}$ when,

$$C_{p_{BASE}} = C_{p_{2-D}} = -\frac{1}{0.91\,M^2 - 0.20\,M + 1.51}$$

(From fig. 5, p. 34, ref. 8)

Body Friction Drag

$$M \le 0.8 \quad \left\{ C_{D_{FB}} = 0.455 \frac{\left[1 + 2\left(\frac{t}{c}\right)_{BODY}\right]\left(\frac{S_{WET}}{S_{REF}}\right)}{(\log_{10} Re)^{2.58}\left(1 + \frac{\gamma - 1}{2} M_o^2\right)^{0.467}} \right.$$

where

$$Re = \rho_o M_o a_o \frac{(MAC)_{BODY}}{\mu_o} \quad \text{and} \quad \left(\frac{t}{c}\right)_{BODY} = \frac{2(l_\pi / l)}{(a/b)\tan \Lambda}$$

$$0.8 < M < 1.2 \left\{ \begin{array}{l} C_{D_{FB}} = \text{linear interpolation with respect to } M \text{ from} \\ \qquad C_{D_{FB}} = C_{D_{FB}} \text{ at } M = 0.8 \text{ to} \\ \qquad C_{D_{FB}} = C_{D_{FB}} \text{ at } M = 1.2 \end{array} \right.$$

$$M \geq 1.2 \left\{ \begin{array}{l} C_{D_{FB}} = C_{D_{FB}} \text{ from numerical integration of local skin-} \\ \qquad \text{friction coefficients on body} \end{array} \right.$$

Body Bluntness Drag

$$M \leq 0.8 \left\{ C_{D_{BB}} = 0 \right.$$

$$0.8 < M < 1.0 \left\{ \begin{array}{l} C_{D_{BB}} = \text{linear interpolation with respect to } M \text{ from} \\ \qquad C_{D_{BB}} = 0 \text{ at } M = 0.8 \text{ to} \\ \qquad C_{D_{BB}} = C_{D_{BB}} \text{ at } M = 1.0 \end{array} \right.$$

$$M \geq 1.0 \left\{ C_{D_{BB}} = \frac{\pi r_{NOSE}^{2}}{S_{REF}} \right.$$

where

$$r_{NOSE}^{0.5} = \frac{1820 \left(\frac{\rho}{\rho_{SL}}\right)^{1/2} (M_{MAX} a 10^{-4})^{3.15}}{\varepsilon_{SKIN} \left(\frac{T_{LE}}{1000}\right)^{4}}$$

ZERO-LIFT FIN DRAG

$$C_{D_{OF}} = C_{D_{pF}} + C_{D_{FF}} + C_{D_{BF}}$$

where

$$C_{D_{X_F}} = C_{D_{X_{\text{HORIZONTAL FINS}}}} + C_{D_{X_{\text{VERTICAL FINS}}}} + C_{D_{X_{\text{CANARD}}}}$$

computed separately by the following equations.

Fin Pressure Drag

$$M \le 0.8 \quad \left\{ \; C_{D_{pF}} = 0 \right.$$

$$0.8 < M < 1.0 \quad \left\{ \begin{array}{l} C_{D_{pF}} = \text{linear interpolation with respect to } M \text{ from} \\ \qquad C_{D_{pF}} = 0 \text{ at } M = 0.8 \text{ to} \\ \qquad C_{D_{pF}} = C_{D_{pF}} \text{ at } M = 1.0 \end{array} \right.$$

$$M = 1.0 \quad \left\{ \; C_{D_{pF}} = 3.4\left(\frac{t}{c}\right)_{FIN}^{5/3} \frac{S_{FIN}}{S_{REF}} \cos^2 \Lambda_{FIN} \right.$$

$$1.0 < M < M_{SA} \quad \left\{ \begin{array}{l} C_{D_{pF}} = \text{linear interpolation with respect to } M \text{ from} \\ \qquad C_{D_{pF}} = C_{D_{pF}} \text{ at } M = 1.0 \text{ to} \\ \qquad C_{D_{pF}} = C_{D_{pF}} \text{ at } M = M_{SA} \end{array} \right.$$

$$M \ge M_{SA} \quad \left\{ \; C_{D_{pF}} = 6\left(\frac{t}{c}\right)_{FIN}^{2} \frac{1}{\beta} \frac{S_{FIN}}{S_{REF}} \right.$$

Fin Friction Drag

$$C_{D_{FF}} = 0.455 \frac{\left[1 + 2\left(\frac{t}{c}\right)_{FIN}\right]\left[\frac{(S_{WET})_{FIN}}{S_{REF}}\right]}{(\log_{10} Re)^{2.58}\left(1 + \frac{\gamma - 1}{2} M_o^2\right)^{0.467}}$$

where

$$Re = \rho_o M_o a_o \frac{(MAC)_{FIN}}{\mu_o}$$

Fin Bluntness Drag

$$M \leq 0.8 \left\{ \; C_{D_{BF}} = 0 \right.$$

$0.8 < M < 1.0$ $\Big\{$ $C_{D_{BF}}$ = linear interpolation with respect to M from
$C_{D_{BF}} = 0$ at $M = 0.8$ to
$C_{D_{BF}} = C_{D_{BF}}$ at $M = 1.0$

$$M \geq 1.0 \left\{ \; C_{D_{BF}} = \frac{8}{3} \frac{r_{LE_{FIN}} b_{FIN}}{S_{REF}} \cos^2 \Lambda_{FIN} \right.$$

where

$$r_{LE_{FIN}} = (0.725 \cos^{1.2} \Lambda_{FIN})^2 r_{NOSE}$$

REFERENCES

1. Gregory, Thomas J.; Petersen, Richard H.; and Wyss, John A.: Performance Tradeoffs and Research Problems for Hypersonic Transports. J. Aircraft, vol. 2, 1965, pp. 266–271.

2. DeYoung, John; and Harper, Charles W.: Theoretical Symmetric Span Loading at Subsonic Speeds for Wings Having Arbitrary Plan Form. NACA Rep. 921, 1948.

3. Lawrence, H. R.: The Lift Distribution on Low Aspect Ratio Wings at Subsonic Speeds. J. Aero. Sci., vol. 18, no. 10, Oct. 1951, pp. 683–695.

4. Puckett, A. E.; and Steward, H. J.: Aerodynamic Performance of Delta Wings at Supersonic Speeds. J. Aero. Sci., vol. 14, no. 10, Oct. 1947, pp. 567–578.

5. McDevitt John B.; Rakich, John V.: The Aerodynamic Characteristics of Several Thick Delta Wings at Mach Numbers to 6 and Angles of Attack to 50. NASA TM X–162,1960.

6. Jorgensen, Leland H.: Elliptic Cones Alone and With Wings at Supersonic Speeds. NACA Rep. 1376, 1958.

7. Van Dyke, Milton D.: The Slender Elliptic Cone as a Model for Nonlinear Supersonic Flow Theory. J. Fluid Mech., vol. 1, May 1956, pp. 1–15.

8. Love, Eugene S.: Base Pressure at Supersonic Speeds on Two-Dimensional Airfoils and on Bodies of Revolution With and Without Fins Having Turbulent Boundary Layers. NACA TN 3819, 1957.

9. Shapiro, Asher: The Dynamics and Thermodynamics of Compressible Fluid Flow. The Ronald Press Co., N. Y., 1954.

10. Koelle, Heinz Hermann: Handbook of Astronautical Engineering. McGraw–Hill Book Co., Inc., 1961.

11. Eckert, Ersnt R. G.: Survey of Heat Transfer at High Speeds. ARL Rep. 189, Aeronaut. Res. Lab., Office of Aerosp. Res., Wright–Patterson Air Force Base, Ohio, Dec. 1961.

12. Truitt, Robert Wesley: Hypersonic Aerodynamics. The Ronald Press Co., N. Y., 1959.

13. Eminton, E.; and Lord, W. T.: Note on the Numerical Evaluation of the Wave Drag of Smooth Slender Bodies Using Optimum Area Distributions for Minimum Wave Drag. J. Roy. Aero. Sco., Jan. 1956, pp. 61–63.

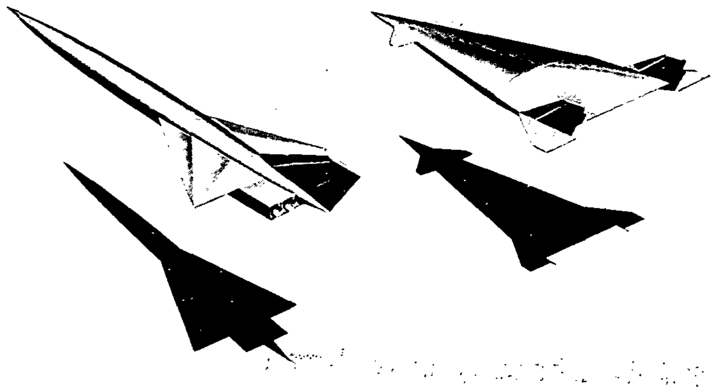

Figure 1.- Aircraft configurations.

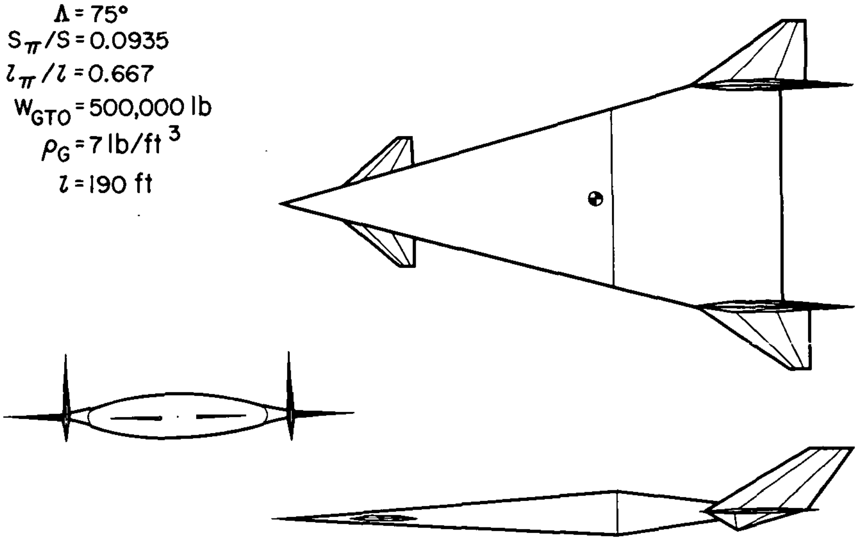

Figure 2.- Nominal configuration; all body cross sections are elliptical.

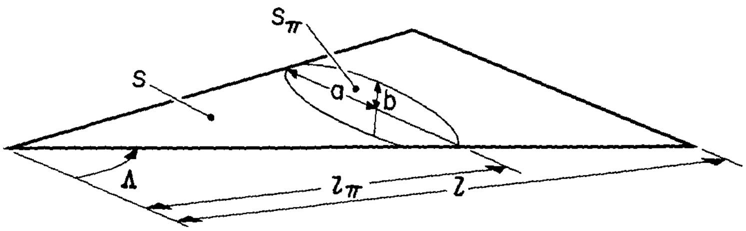

$$\frac{a}{b} = \frac{\pi(l_\pi/l)^2 \cot \Lambda}{(S_\pi/S)}$$

Figure 3.- Body shape parameters.

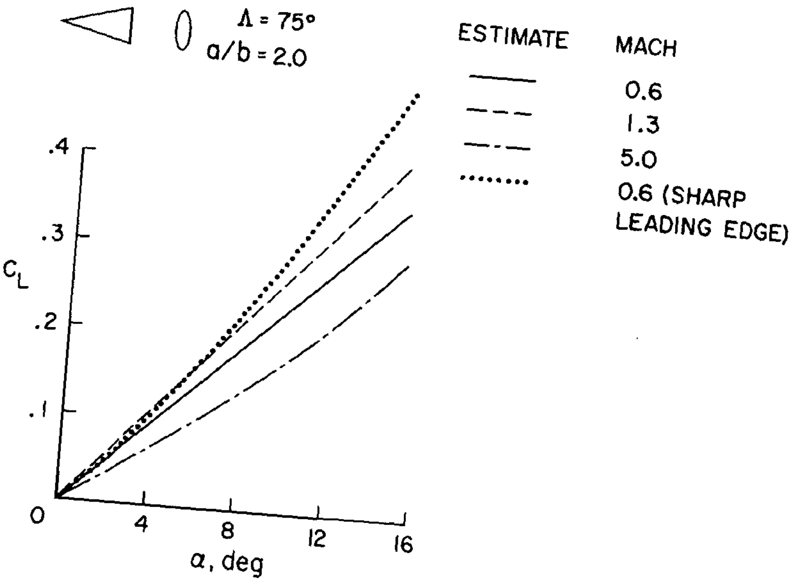

Figure 4.- Effect of Mach number on lift.

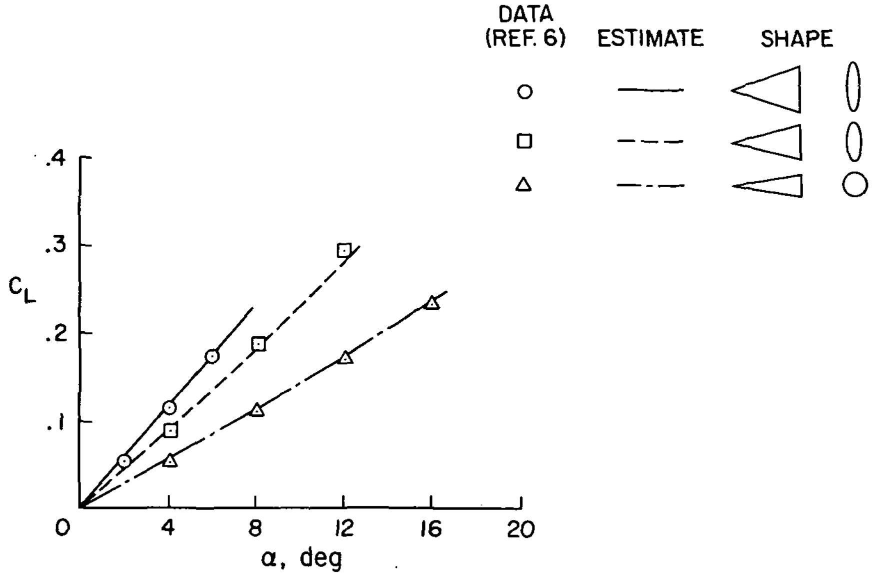

Figure 5.- Effect of shape on lift; M = 1.97.

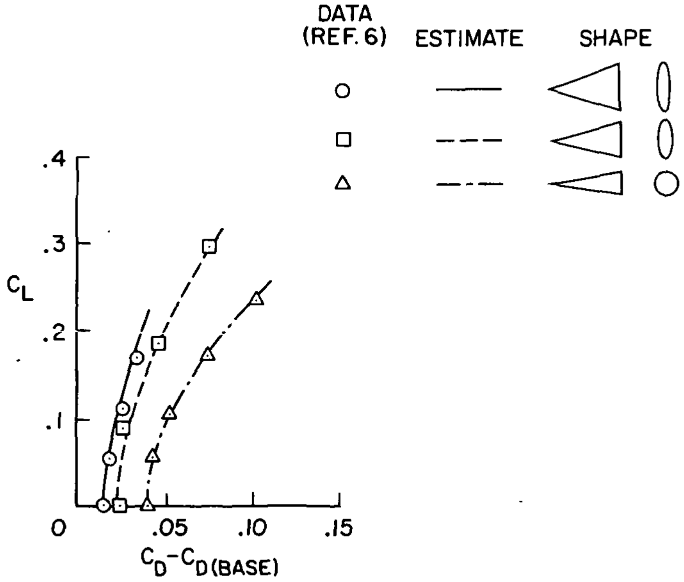

Figure 6.- Effect of shape on induced drag; M = 1.97.

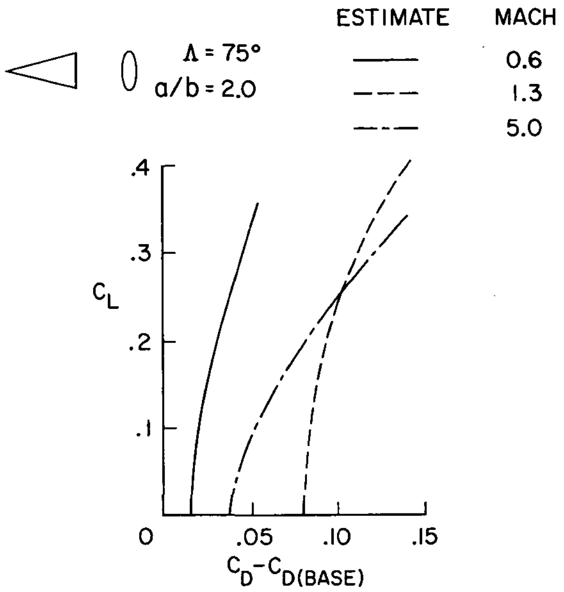

Figure 7.- Effect of Mach number on induced drag.

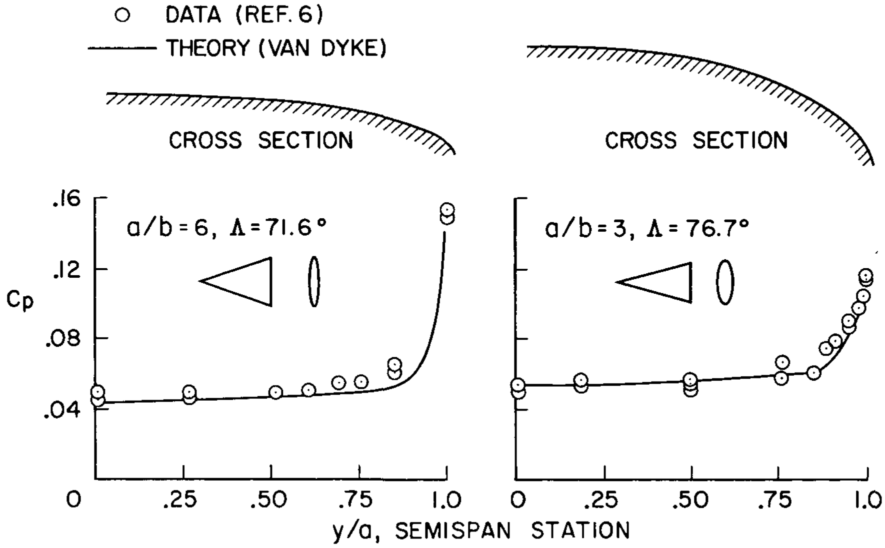

Figure 8.- Forebody pressure distribution; M = 1.97, α = 0°.

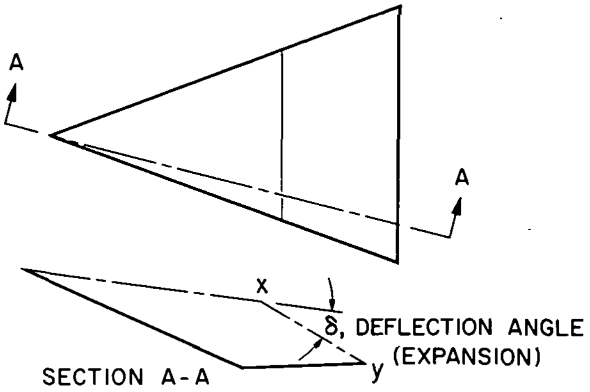

Figure 9.- Afterbody-pressure-calculation geometry.

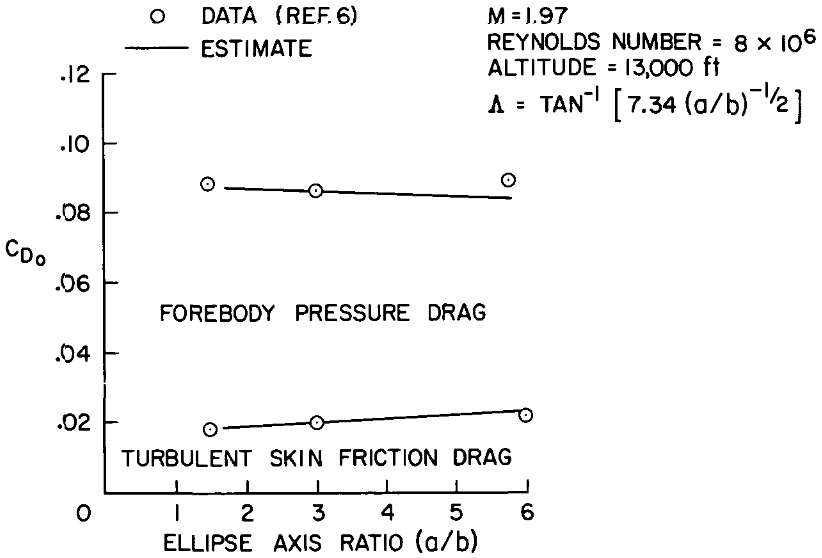

Figure 10.- Comparison of forebody zero-lift drag with experiment; no base drag is included; C_{D_o} is based on cross-section area.

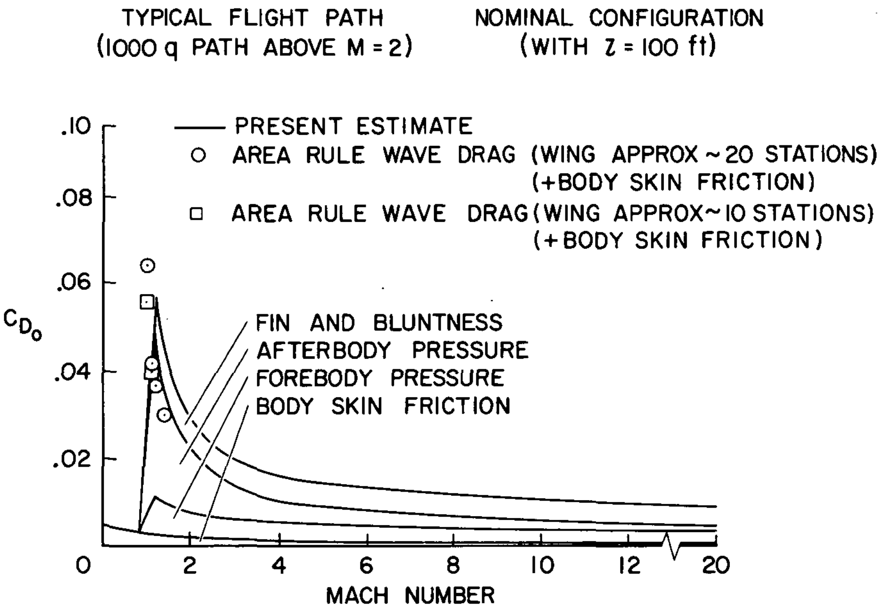

Figure 11.- Zero-lift drag versus Mach number; C_{D_o} is based on theoretical body plan area.

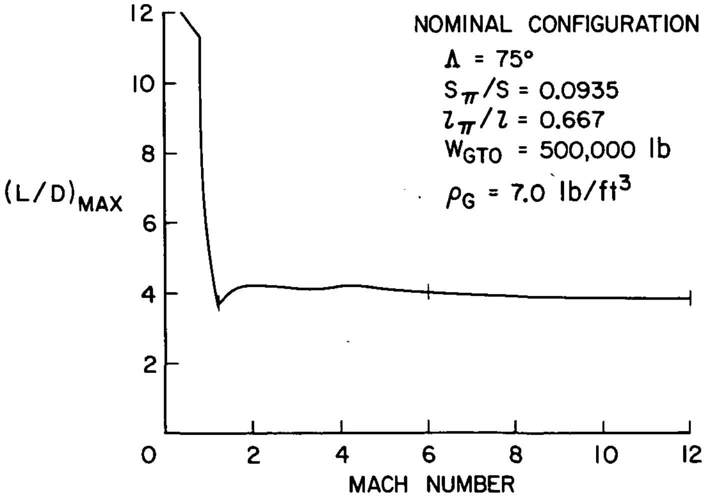

Figure 12.- Effect of Mach number on $(L/D)_{MAX}$.

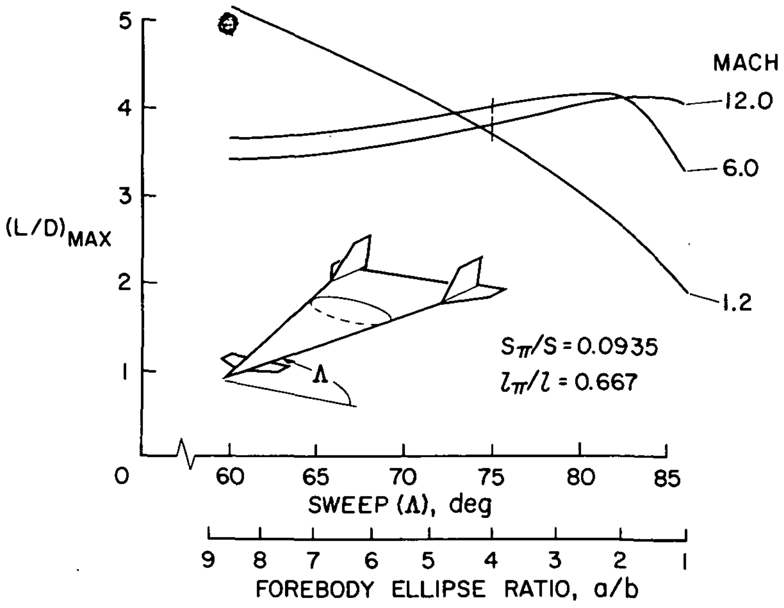

Figure 13.- Effect of body sweep on (L/D)$_{MAX}$.

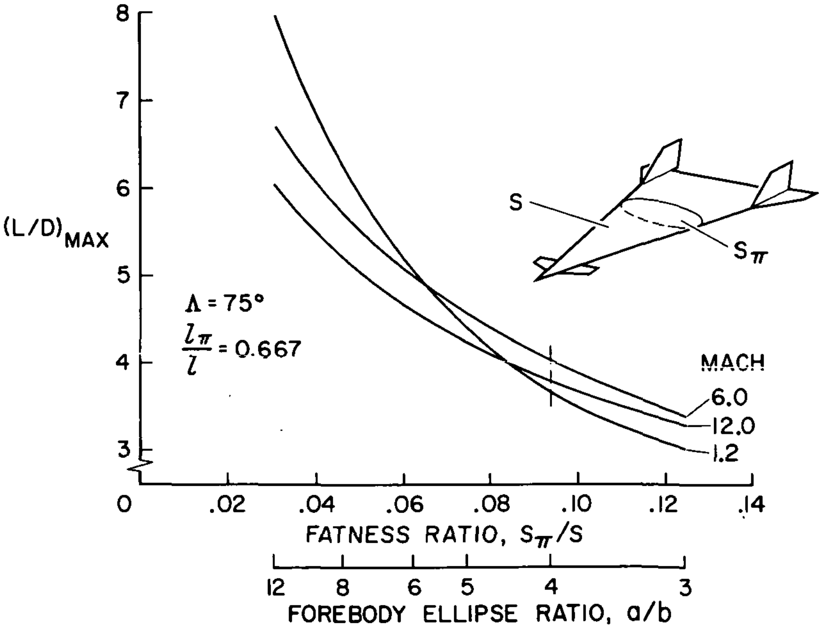

Figure 14.- Effect of fatness ratio on (L/D)$_{MAX}$.

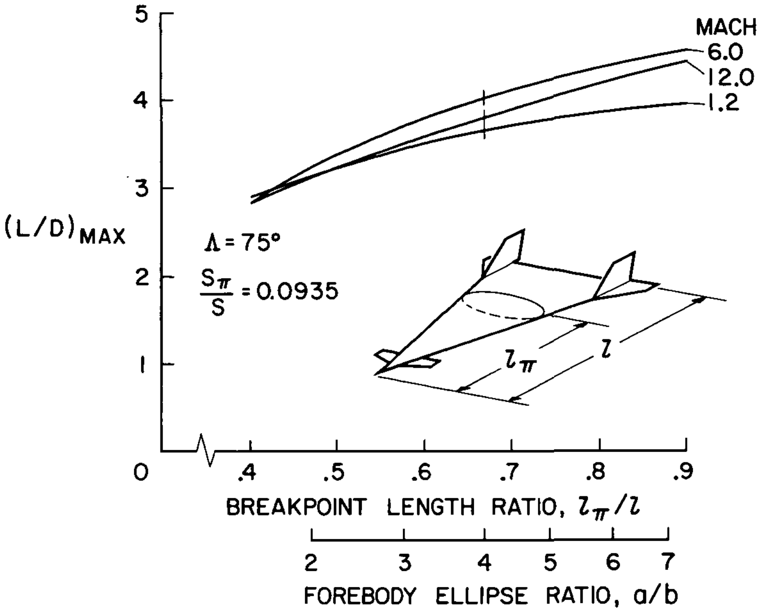

Figure 15.- Effect of breakpoint length ratio on $(L/D)_{MAX}$.

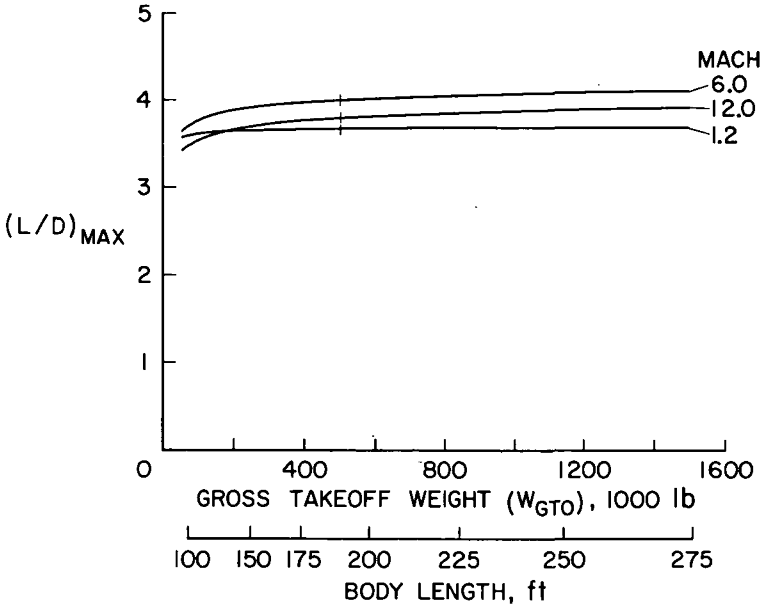

Figure 16.- Effect of gross takeoff weight on $(L/D)_{MAX}$; gross body density = 7.0 lb/ft^3.

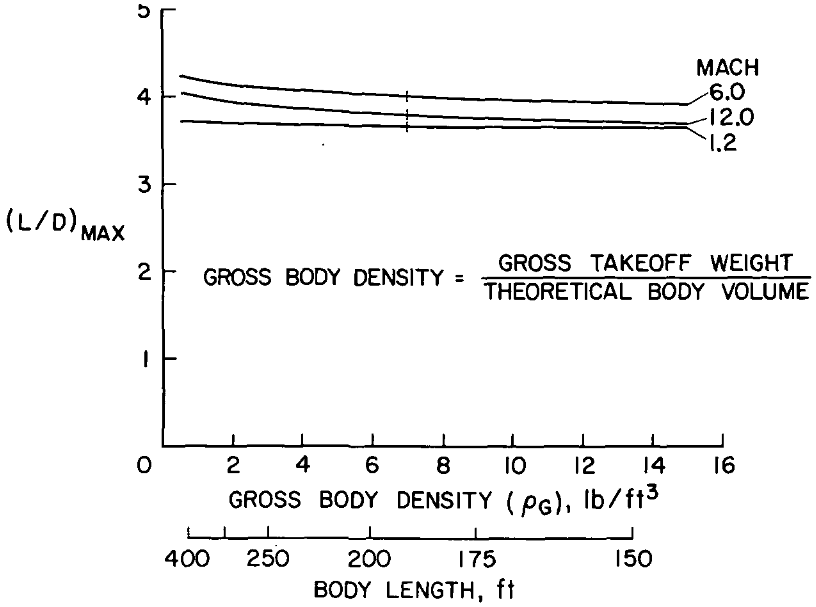

Figure 17.- Effect of gross body density on $(L/D)_{MAX}$; gross takeoff weight = 500,000 lb.

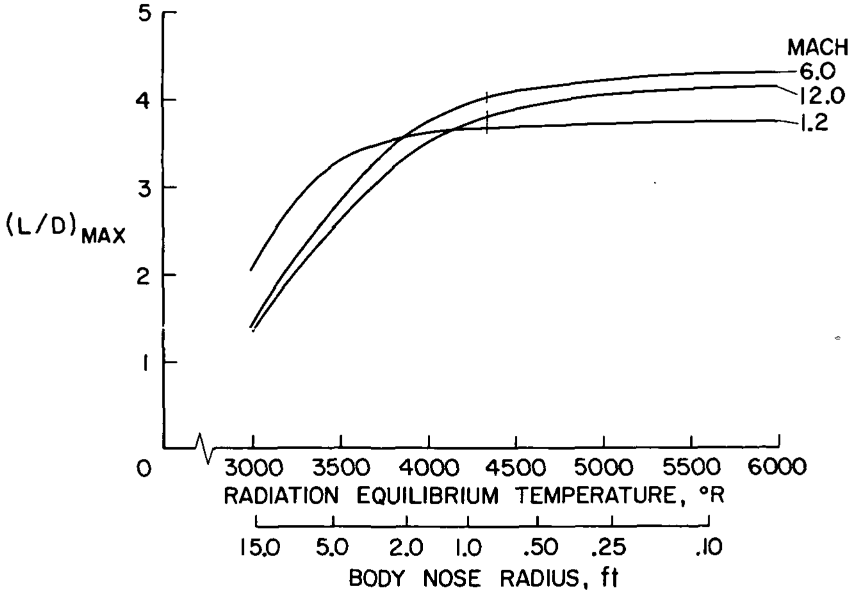

Figure 18.- Effect of maximum allowable leading-edge temperature.

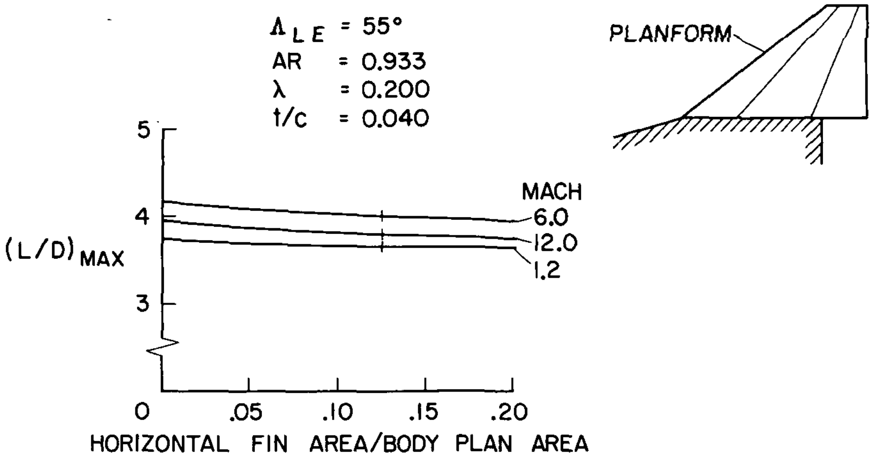

Figure 19.- Effect of horizontal fin size on $(L/D)_{MAX}$; maximum leading-edge temperature = 4350° R.

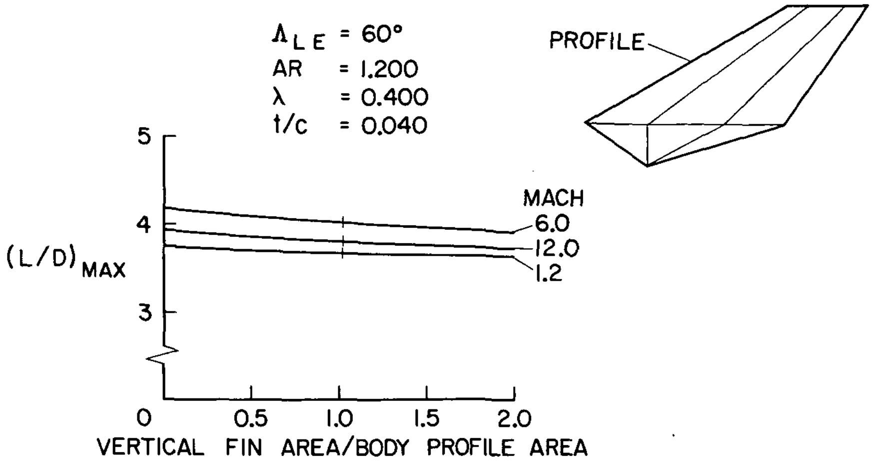

Figure 20.- Effect of vertical fin size on $(L/D)_{MAX}$; maximum leading-edge temperature = 4350° R.

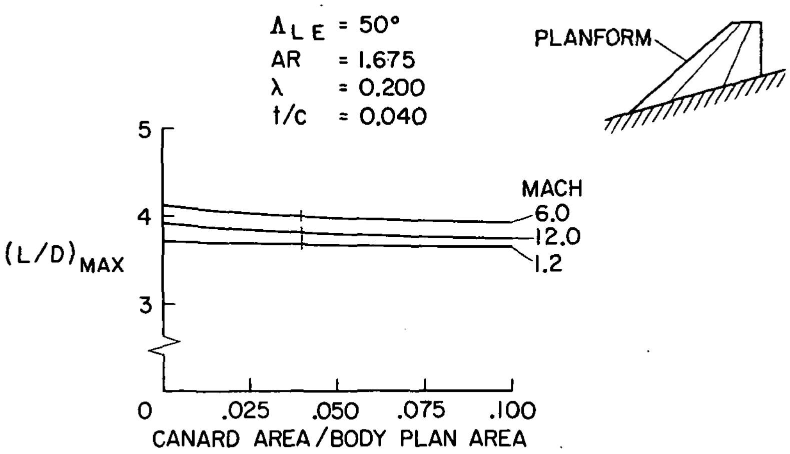

Figure 21.- Effect of canard size on $(L/D)_{MAX}$; maximum leading-edge temperature = 4350° R.

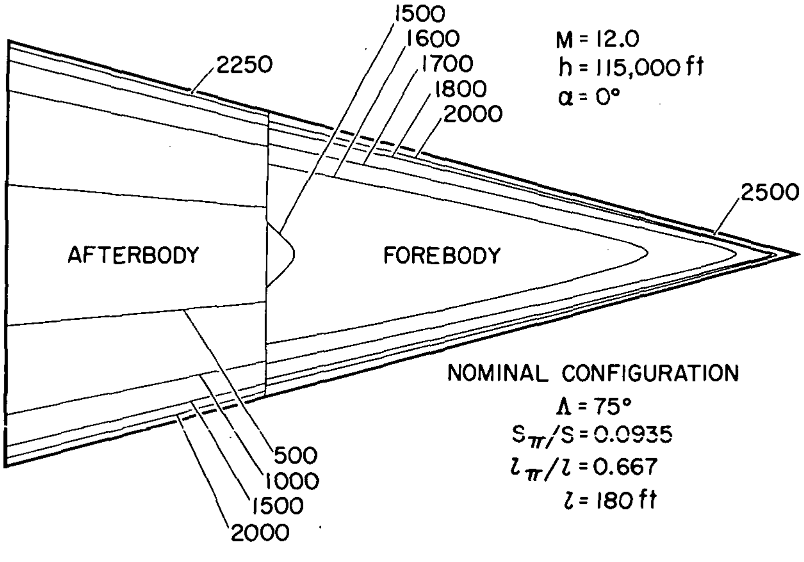

Figure 22.- Planform temperature contours, °F.

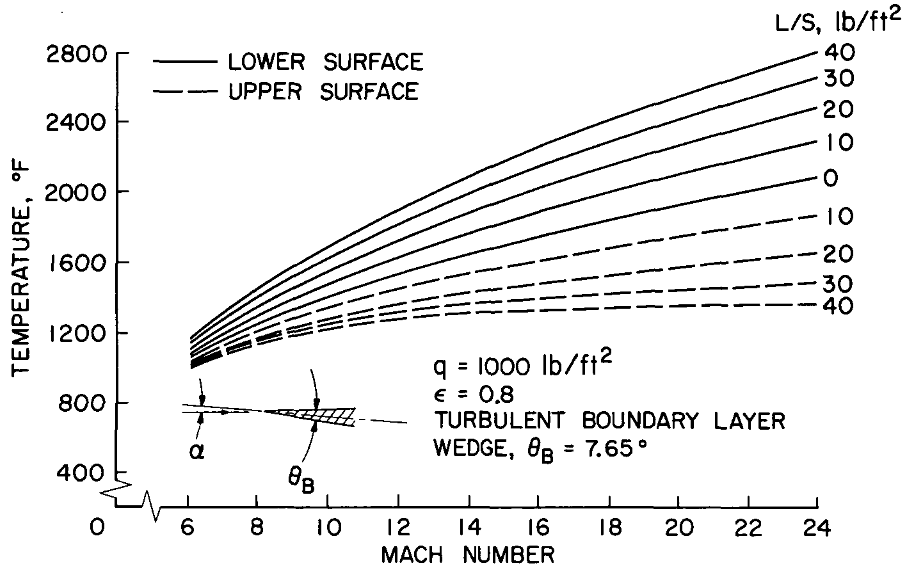

Figure 23.- Surface radiation equilibrium temperature; 25 feet aft of leading edge.

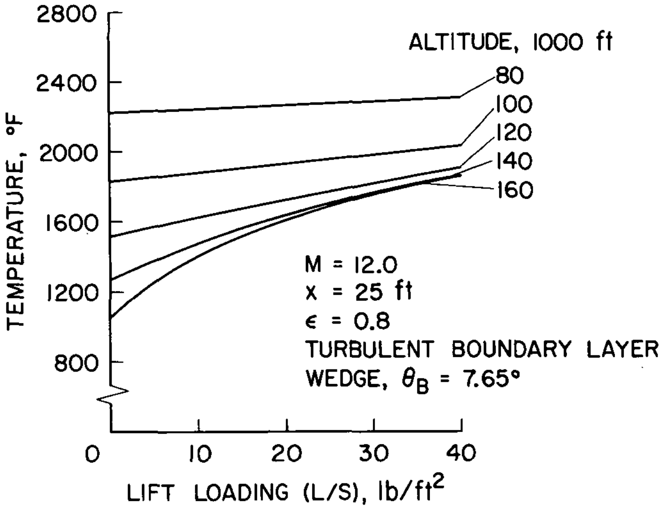

Figure 24.- Effect of altitude and lift loading on lower surface temperature.

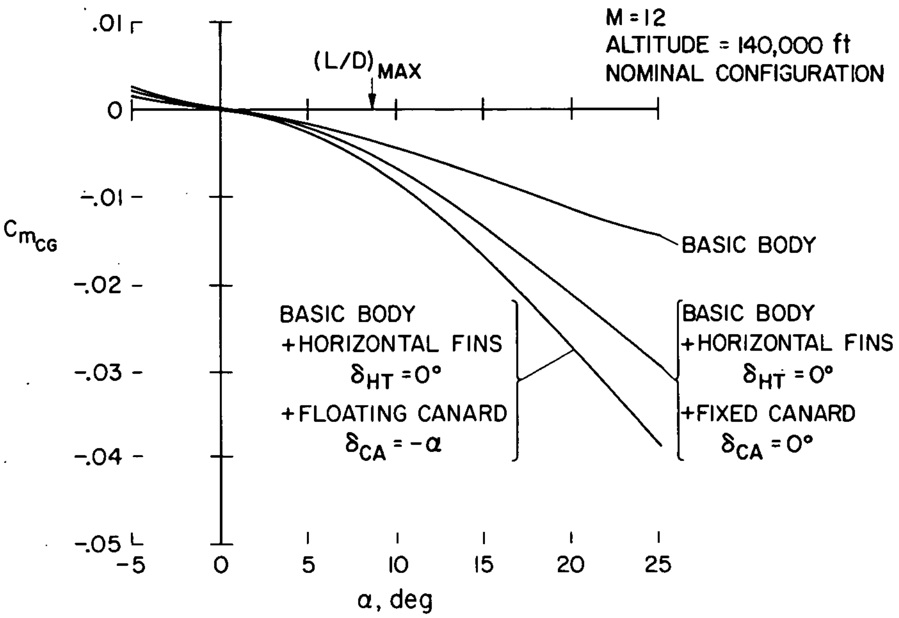

Figure 25.- Longitudinal stability.

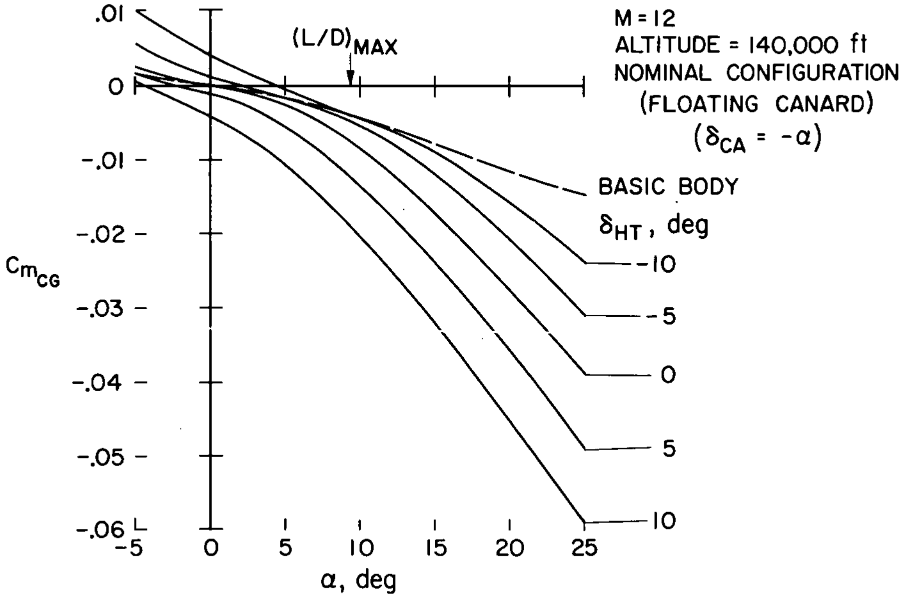

Figure 26.- Horizontal fin control power.

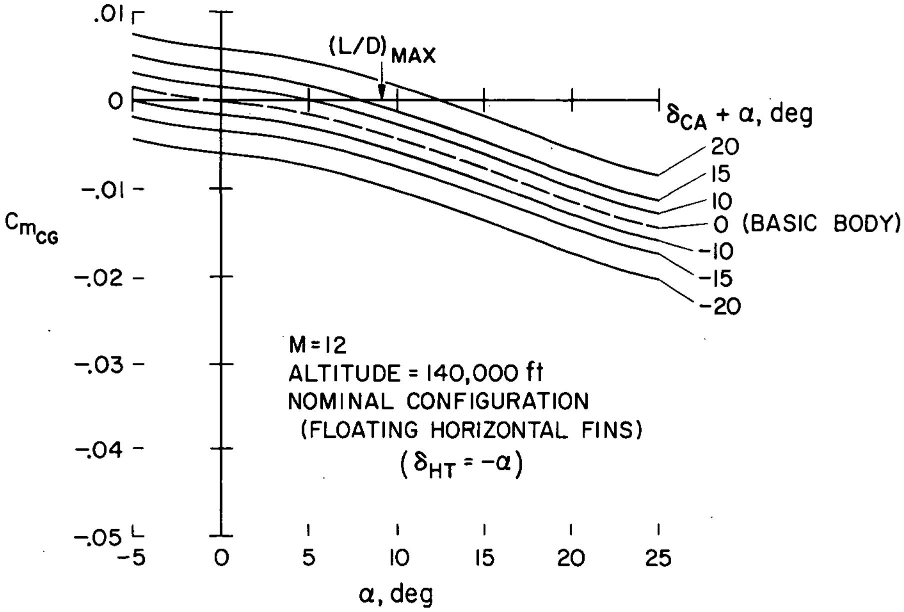

Figure 27.- Floating canard control power.

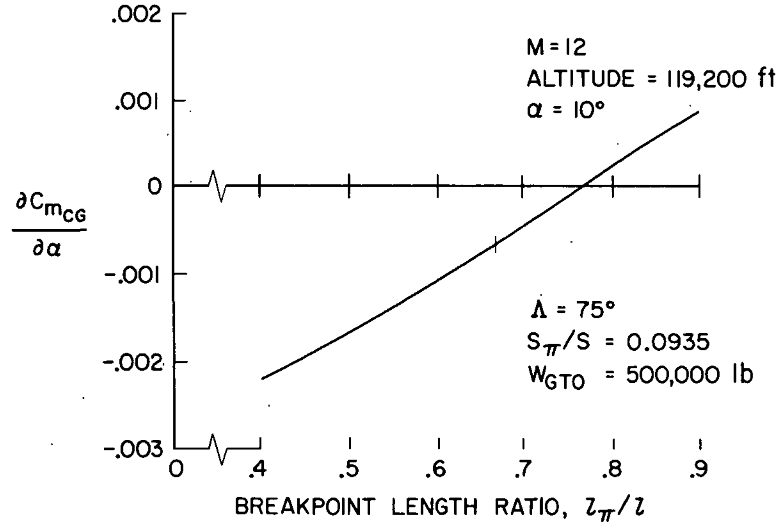

Figure 28.- Effect of body shape on stability.

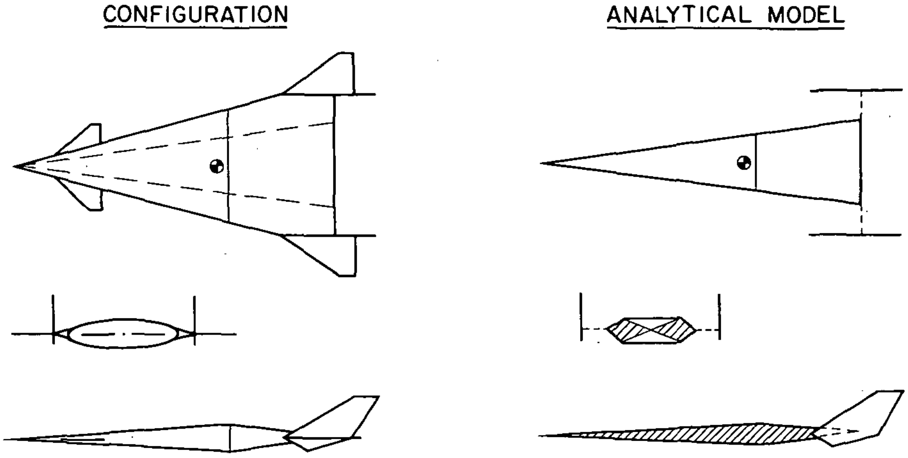

Figure 29.- Directional stability model.

NASA-Langley, 1971 —— 1 A-3637

> *"The aeronautical and space activities of the United States shall be conducted so as to contribute . . . to the expansion of human knowledge of phenomena in the atmosphere and space. The Administration shall provide for the widest practicable and appropriate dissemination of information concerning its activities and the results thereof."*
>
> —NATIONAL AERONAUTICS AND SPACE ACT OF 1958

NASA SCIENTIFIC AND TECHNICAL PUBLICATIONS

TECHNICAL REPORTS: Scientific and technical information considered important, complete, and a lasting contribution to existing knowledge.

TECHNICAL NOTES: Information less broad in scope but nevertheless of importance as a contribution to existing knowledge.

TECHNICAL MEMORANDUMS: Information receiving limited distribution because of preliminary data, security classification, or other reasons.

CONTRACTOR REPORTS: Scientific and technical information generated under a NASA contract or grant and considered an important contribution to existing knowledge.

TECHNICAL TRANSLATIONS: Information published in a foreign language considered to merit NASA distribution in English.

SPECIAL PUBLICATIONS: Information derived from or of value to NASA activities. Publications include conference proceedings, monographs, data compilations, handbooks, sourcebooks, and special bibliographies.

TECHNOLOGY UTILIZATION PUBLICATIONS: Information on technology used by NASA that may be of particular interest in commercial and other non-aerospace applications. Publications include Tech Briefs, Technology Utilization Reports and Technology Surveys.

Details on the availability of these publications may be obtained from:

SCIENTIFIC AND TECHNICAL INFORMATION OFFICE

NATIONAL AERONAUTICS AND SPACE ADMINISTRATION

Washington, D.C. 20546